Received: 22 August 2021 | Revised: 22 January 2022 | Accepted: 7 March 2022

DOI: 10.1002/ldr.4261

RESEARCH ARTICLE

WILEY

# High-resolution mapping of soil pollution by Cu and Ni at a polar industrial barren area using proximal and remote sensing

Yury Dvornikov[1] | Marina Slukovskaya[1,2,3] | Alexey Yaroslavtsev[1,4] | Joulia Meshalkina[4,5] | Alexey Ryazanov[1] | Dmitrii Sarzhanov[1] | Vyacheslav Vasenev[6]

[1]Department of Landscape Design and Sustainable Ecosystems Agrarian-Technological Institute, Peoples' Friendship University of Russia, Moscow, Russia

[2]Tananaev Institute of Chemistry and Technology of Rare Elements and Mineral Raw Materials, Kola Science Centre, Russian Academy of Sciences, Apatity, Russia

[3]Laboratory of Nature-inspired Technologies and Environmental Safety of the Arctic region, Kola Science Centre, Russian Academy of Sciences, Apatity, Russia

[4]Department of Ecology, Russian State Agrarian University - Moscow Timiryazev Agricultural Academy, Moscow, Russia

[5]Soil Science Faculty, Lomonosov Moscow State University, Moscow, Russia

[6]Soil Geography and Landscape Group, Wageningen University, Wageningen, The Netherlands

**Correspondence**

Yury Dvornikov, Department of Landscape Design and Sustainable Ecosystems Agrarian-Technological Institute, Peoples' Friendship University of Russia, Miklukho-Maklaya, 6, Moscow 117198, Russia.
Email: ydvornikow@gmail.com

**Funding information**

RUDN University Strategic Academic Leadership Program; Russian Science Foundation, Grant/Award Number: 19-77-300-12; Russian Foundation for Basic Research, Grant/Award Number: 19-29-05187

## Abstract

Industrial pollution by potentially toxic elements (PTE) remains a key environmental threat, resulting in soil and ecosystem degradation. Remediation of the industrial barrens is challenging in polar regions, where plant growth is hampered by severe climatic conditions. High-resolution mapping of soil pollution is needed to support soil remediation and management projects. The distribution of nickel (Ni) and copper (Cu) was analyzed in the topsoil within the industrial barren around the Ni and Cu smelter in Kola Peninsula, Russia using a field-portable XRF analyzer. Bulk Cu and Ni contents were measured at 84 observation points within the area of two hectares planned for remediation. The PTE content varied between 0.2 and 9.0 g $kg^{-1}$ for Cu and between 0.2 and 21 g $kg^{-1}$ for Ni. The area was surveyed with unmanned aerial vehicles and differential global navigation satellite systems to obtain a high-accuracy digital terrain model for exploring the factors behind the spatial variability. Field observations were interpolated by regression kriging with different input resolution of auxiliary data (0.5–1.0–1.5–2.0 m) and different regression models (gradient boosting machines and multiple linear regression). Model performance and validation showed that 1.0–1.5 m resolution of auxiliary data were the best for projecting Cu and Ni topsoil contents within the study site. The soil type and topographic wetness index were the most important variables explaining Cu and Ni content variability.

KEYWORDS

gradient boosting machines, industrial barren area, polar regions, potentially toxic metals, technogenic soils, unmanned aerial vehicle

## 1 | INTRODUCTION

Industrial pollution leads to severe environmental circumstances globally, especially in regions where unfavorable climatic conditions constrain ecosystem restoration. In polar regions, long-term intensive soil pollution by potentially toxic elements (PTE) results in the formation of industrial barrens - bleak open landscapes (foliage projective cover less than 10%) evolved around the point sources of industrial pollution (Kozlov & Zvereva, 2007). A significant part of more than 40 globally recognized industrial barrens was formed due to the activity of non-ferrous industrial plants and their aerial emissions. The industrial barren formed because of the influence of the copper-nickel smelter in the vicinity of Monchegorsk at the Kola Peninsula is one of the World's largest. The Cu-Ni smelter [Kola Mining and Metallurgical Company ( MMC), former «Severonickel»] is among the leading global producers of nickel, copper, and cobalt and, therefore, one of the most significant sources of metal emissions in Northern Europe. Founded in 1938, the MMC plant is active nowadays, and its annual emissions estimated up to 40 Gg are deposited on vast areas about 300 km distance from the source (Nikanov et al., 2020; Slukovskaya, Vasenev, et al., 2020). The measures taken in 1999 under the environmental protection strategy reduced the gross emissions of non-soluble metal compounds to 1608–1780 t for Ni and 877–1096 t Cu reported during recent years (Nikanov et al., 2020). Nevertheless, soils at the industrial barren in the impact zone of the plant remain heavily contaminated by Cu and Ni because of long-term emissions. The content of PTE in the topsoil can reach extremely high values which are comparable to the processed Cu/Ni ore (Ni – 0.24%–4.2%, Cu – 0.36%–5.8%) (Kashulina, 2017) and exceed the health thresholds and background content by 1–3 orders of magnitude (Kashulina, 2018).

Several attempts have already been made to investigate the spatial distribution and temporal dynamics of the PTE in soils of the industrial barren at sites located up to 75 km away from the smelter (Kashulina, 2017, 2018; Lyanguzova et al., 2016), and an exponential decrease in the contaminants' content with the distance from the pollution source was reported (Lyanguzova et al., 2016). Although the general patterns in spatial–temporal variability of soil pollution at the industrial barren were described, there are still gaps in quantitative assessments of local variations related to topography, soil types and properties. Considering a hilly meso-relief and a complex structure of soil cover, including Histosols and Podzols, the existing gaps hamper the accuracy of the PTE maps and limit their value for remediation planning.

High-resolution mapping by conventional soil survey approaches and soil analysis in chemical laboratories (e.g., by atomic absorption or ionic coupled plasma spectrometry) is hardly applicable for the area of industrial barren due to high costs and long time needed for analysis. Smart technologies of proximal sensing, including remote sensing and express non-destructive measurements, can provide an alternative fast and cost-effective solution (Shi et al., 2018). Proximal sensing is widely used for express analysis and mapping contents of nutrients, salts or PTEs in soils (Guo et al., 2015; Hong et al., 2019; Nouri et al., 2018). Portable X-ray fluorescence (pXRF) spectrometry provides an opportunity to measure the bulk concentration of PTEs in the field with minimal sample preparation and relatively high accuracy (Qu et al., 2019; Sacristán et al., 2016; Xia et al., 2019). Unmanned aerial vehicles (UAV) with multispectral and hyperspectral cameras enable direct (through spectral properties of polluted soils) and indirect (through the spectral signatures of pollution-induced constrains for the vegetation growth) (Gholizadeh & Kopačková, 2019) mapping of the PTE contents in soils (Boente et al., 2020; Tan et al., 2020). Given the quasi-complete absence of vegetation (ca. 10%) within industrial barrens (Kozlov & Zvereva, 2007), a high-accuracy digital terrain model (DTM) can be derived based on photogrammetric processing of UAV data to analyze the effect of micro- and meso-topographic features and associated soil patterns on the PTE distribution. Since the distribution of PTE in soils are geographically determined and may closely be related to other environmental variables (proxies), the combination of geostatistical and non-geostatistical methods can be considered as an optimal approach to achieve high mapping accuracy (Li & Heap, 2014; Zhu & Lin, 2010). Non-linear models shall be preferred considering the non-linear interactions between the landscape components. However, the overall interpolation accuracy would depend on the number of input observation points and the output resolution of the interpolation grid (Hengl, 2006).

This paper aimed to: i) assess spatial variations of Cu/Ni topsoil content at a high spatial resolution based on the remote UAV and proximal sensing; ii) explore the topographic variables as a potential proxy for mapping Cu/Ni contents at the industrial barren considering topographic and soil patterns; iii) test the effect of the input data resolution and different interpolation models on the accuracy of the soil pollution maps at the industrial barren.

## 2 | MATERIALS AND METHODS

### 2.1 | Study site description

The research area is located on the Kola Peninsula north of the Polar Circle. The regional subArctic climate is considered cold with no dry season and cold summers (Dfc according to updated Köppen-Geiger classification, [Beck et al., 2018]). The native vegetation of the area around Kola MMC before the smelter establishment was dominated by northern *taiga* species: *Picea abies* and *Pinus sylvestris* (Manninen et al., 2015). Leptic Albic/Entic Podzol is a dominating soil type in the area.

The study site (67.9 N, 32.8E) is in the vicinity of Monchegorsk situated at 1.5 kilometres north of the pollution source within the impact zone of the smelter (Figure 1). The study site is a two-hectare area of a typical industrial barren. This area was developed over decades of industrial pollution resulting in the complete degradation of the plant cover (Kryuchkov, 1993). Naturally, the territory belongs to the northern boundary of the northern *taiga* zone. However, the studied industrial area was only sparsely vegetated with the domination of *Salix* L. sp. and *Betula pubescens* Ehrh. trees (Koptsik et al., 2016). The site has a diverse meso-topography, including the top of the hill, hill slopes, and two local depressions. The prevailing soil types are Skeletic Leptic Entic Podzol (Arenic, Toxic) (hilltop and slopes) (further – Podzol) and Dystric Rheic Hemic Histosol (Toxic) (local depressions) (further - Histosol), according to IUSS World Reference Base (IUSS Working Group, 2015). A remediation project implemented on the part of the site in 2003 included covering the degraded Podzol subsoils by valley peat (Koptsik et al., 2016). It resulted in forming semi-natural soil, which we identified as Skeletic Leptic Entic Podzol (Arenic, Organotransportic, Toxic) (further – Histosol/Podzol). The identified soil types differed in the capacity to accumulate the PTE and the ratio of soluble and non-soluble forms of metals. In the Podzol, Ni was mainly accumulated in non-soluble forms with the bioavailability of 1.5%, while Cu was predominantly (60%) available for plants (Slukovskaya et al., 2019). Metal bioavailability in the Histosol was 19% for Ni and 57% for Cu (Slukovskaya, Kremenetskaya, et al., 2020).

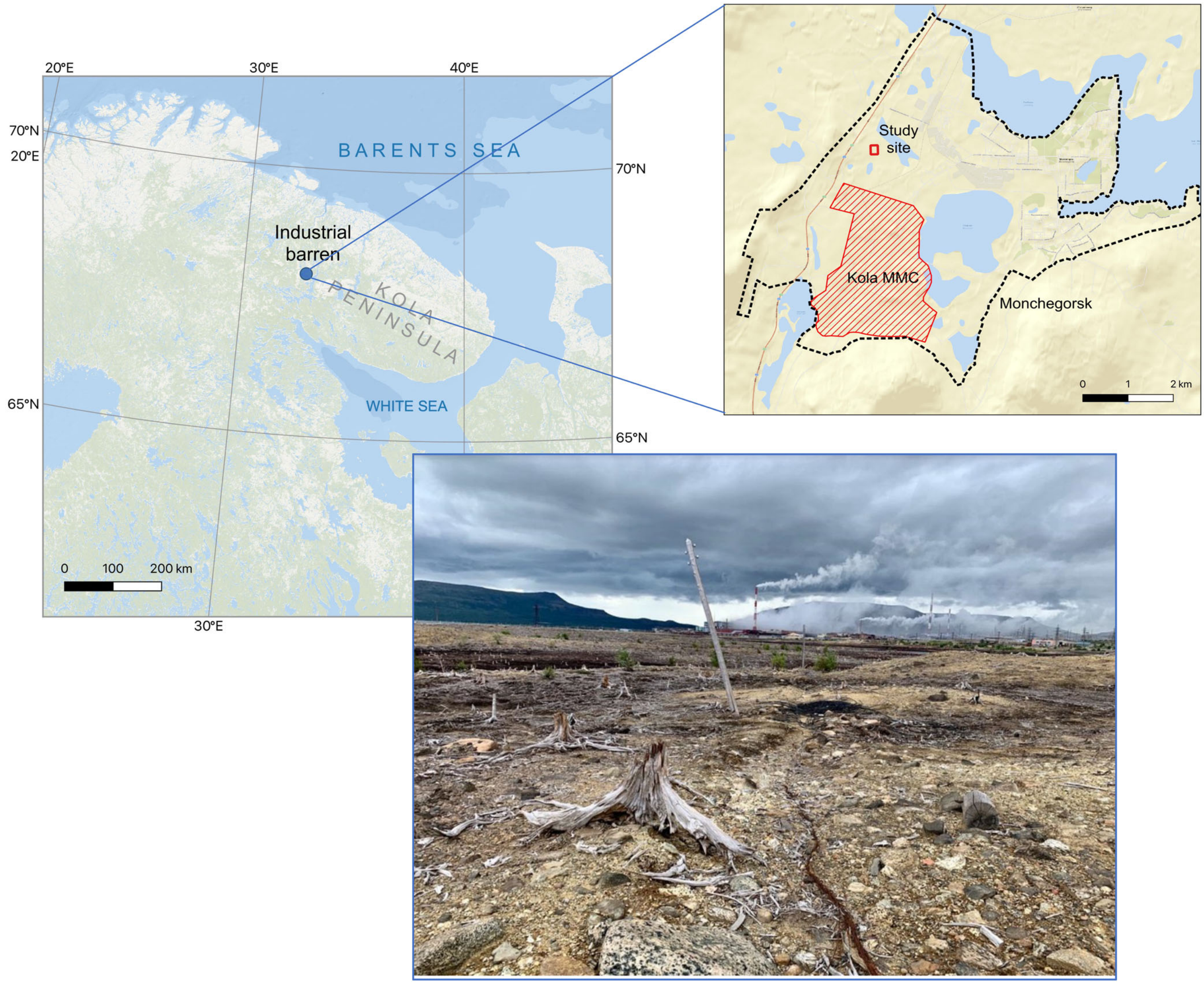


**FIGURE 1** Monchegorsk industrial barren (ESRI© Basemap layers, photo of the author dated to July 2020) [Colour figure can be viewed at wileyonlinelibrary.com]

## 2.2 | Field survey

The observation locations were selected based on a random stratified design. The area was subdivided into 20 m by 20 m grids and 1–2 observation locations inside each grid cell were randomly selected (84 in total). Bulk concentrations of Cu and Ni in soil surface were measured in the field using the Olympus Vanta portable X-ray fluorescence analyzer (pXRF). The pXRF analyzer was placed on top of a clear plastic bag on the desired location (to protect the lens from contamination) to take measurements within 60 s exposure time. The pXRF analyzes an area of 10 $mm^2$ and penetrates to a depth of 2 mm (Kalnicky & Singhvi, 2001). The maximal measurement error did not exceed 3%, according to the internal instrument assessment. The observation locations were selected randomly but with the aim to cover all geomorphological units such as slopes, hilltop, small valleys and depressions, and various soil types. In addition, soil samples from 84 locations were taken for the determination of soil carbon content, pH and bulk density in the laboratory. The soil samples were grouped by soil type: 'Podzol', 'Histosol' and 'Histosol/Podzol'.

The land cover of the site was surveyed with the drone DJI Mavic 2 Pro equipped with Hasselblad 20 MP resolution and ~77 degree viewing angle camera. Overflights were organized through DroneDeploy© software. Input flight parameters were set to 3 m $s^{-1}$ speed, 90 m flight altitude, front overlap – 90%, lateral overlap – 85%. In total, 123 images 5472 × 3648 px covering the entire study site were taken.

Differential global navigation satellite system (GNSS) survey within the study area was performed using STONEX© S9III differential GPS/Glonass in RTK mode. This method allows measuring point coordinates with the plane and vertical accuracies of 1 and 2 cm, respectively. During the survey, we have measured geospatial coordinates and elevations of each observation point ($n$ = 84) as well as of the additional ground control points (GCP) for the UAV survey ($n$ = 5) and of additional points within the study site for better representation of topography ($n$ = 105).

## 2.3 | Topographic data

Raw UAV survey data were processed within AGISOFTt© Metashape Professional 1.6.4 software to obtain a high accuracy digital surface model (DSM). The measured GCPs were incorporated into the project for improving spatial and vertical accuracy. Vegetation was filtered using the internal software algorithm. The filtered DSM was further re-projected into UTM Zone 36 N projection (datum WGS-84), resampled to the spatial resolution of 0.5 m, and exported as GeoTIFF. This DSM was further improved to obtain a hydrologically correct representation of the terrain. From the exported raster, contours were extracted at 0.2 m intervals, and all contours were manually corrected and cleaned from artifacts related to misclassified vegetation. An improved digital terrain model (DTM) was created by interpolating corrected contours and measured points (preference in the interpolation) using TopoToRaster algorithm with drainage enforcement (Hutchinson, 1989) within the ESRI© ARC GIS 10.2 software. The improved DTM was produced at four different spatial resolutions: 0.5, 1.0, 1.5, and 2.0 m, to test how the input resolution influences the interpolation of Cu and Ni content values, similarly to Florinsky & Kuryakova (2000). Several topographic variables were obtained: slopes, aspects, total curvature, flow direction, flow accumulation, and topographic wetness index (TWI) as derivatives from the DTM. All topographic variables were calculated within the R environment (R Core Team, 2017) using packages ‘raster’ (Robert & van Etten, 2012), ‘dynatopmodel’ (Quinn et al., 1995) and ‘spatialEco’ (Evans, 2020).

## 2.4 | Environmental variables

In total, we have compiled eight environmental variables that were further used as predictors within the multiple linear regression (MLR) and gradient boosting machines (GBM). Most of them are topographic variables ($n = 7$): elevation (m), slopes (degrees), aspect (degrees), total curvature, TWI, flow direction, and flow accumulation. Total curvature represents the convexity and concavity degree of topographic patterns, that is, one raster cell relative to the other eight surrounding raster cells (Zeverbergen & Thorne, 1987). Negative curvature values correspond to concave and positive to convex patterns. TWI is an index that combines local upslope contributing area and slope, representing the interconnection between topography and hydrology (Beven & Kirkby, 1979). It quantifies the potential amount of surface inflow that can be drained through and accumulated in each raster cell: higher index values belong to flat depressions whereas low – to hilltops and steep hill slopes. Flow direction raster is a numerical clockwise coding of the drainage and is calculated for each cell according to the difference between the elevation of the target cell compared to eight neighbouring cells (Jenson & Domingue, 1988). Flow accumulation is a quantitative assessment of the cell amount that can potentially be drained through the target cell (Jenson & Domingue, 1988). Another variable, ‘soil types’, was mapped by digitizing manually the orthophotographs and using the field descriptions. Based on the previous soil surveys, these types were coded as ‘Podzol’, ‘Histosol’, and ‘Histosol/Podzol’. All data were presented as float values except soil type (factor 1–3) and flow direction (integer).

## 2.5 | Statistical processing and regression kriging

We have chosen the regression kriging as an approach for Cu/Ni data interpolation within the study site. The approach included the multiple linear/non-linear regression model fitting between dependent variables (Cu/Ni contents) and independent explanatory variables followed by the kriging of regression residuals.

Entire Cu/Ni experimental dataset ($n = 84$) was randomly divided into two sets: 1) training (80%) and 2) test (20%). Training data were used within regression kriging (RK) and test dataset – for quality assessment. Response variables (Cu and Ni contents in the topsoil) were square-root – transformed prior to the analysis to fulfill the normality distribution requirement for the linear regression models.

To explain the deterministic part of variations for Cu and Ni, two regression modeling approaches were initially chosen: MLR and GBM available within ‘caret’ package in the R environment (R Core Team, 2017). Seven-fold cross-validation was applied to both models to avoid biases. We assessed the regression model's performance using two criteria: adjusted $R^2$ ($R^2_{adj}$) and prediction root-mean-squared error (RMSE). $R^2_{adj}$ was calculated as follows:

$$1-\left(1-R^2\right)\times[(n\text{-}1)/(n\text{-}p\text{-}1)],$$

*Where:* $R^2$ is calculated as the sum of squares of fitted values divided by sum of squares of the observed values, n is the number of observations ($n = 68$ for the training set), p is the number of predictors used within the model. Model RMSE was calculated as follows:

$$\left[\left(\sum(\mathrm{f}-\mathrm{o})\hat{}2/\mathrm{n}\right)\hat{}0.5\right],$$

*Where:* f is a vector of fitted values and o is a vector of observed values. Residuals from the final MLR and GBM models (for Cu and for Ni) were further used in variogram fitting and kriging. Variograms for MLR and GBM residuals were fitted using the ‘gstat’ package (Gräler et al., 2016) within the R environment (R Core Team, 2017). Exponential models were used to fit all variograms. The mean kriging variance (kriging RMSE) was calculated for each of interpolated raster and included in the quality metrics assessment at the validation stage.

At the validation stage, all obtained maps were converted from square root values into original Cu/Ni content values, and interpolated values were extracted for quality control for each test point ($n = 16$). We have assessed the following map quality indexes (Wadoux & Brus, 2021): mean absolute error (MAE), RMSE, and $R^2$ of observed (test dataset) and interpolated Cu/Ni content values. The scheme of the workflow is presented in Figure 2.

**FIGURE 2** Workflow scheme of models' calibration and validation of final maps

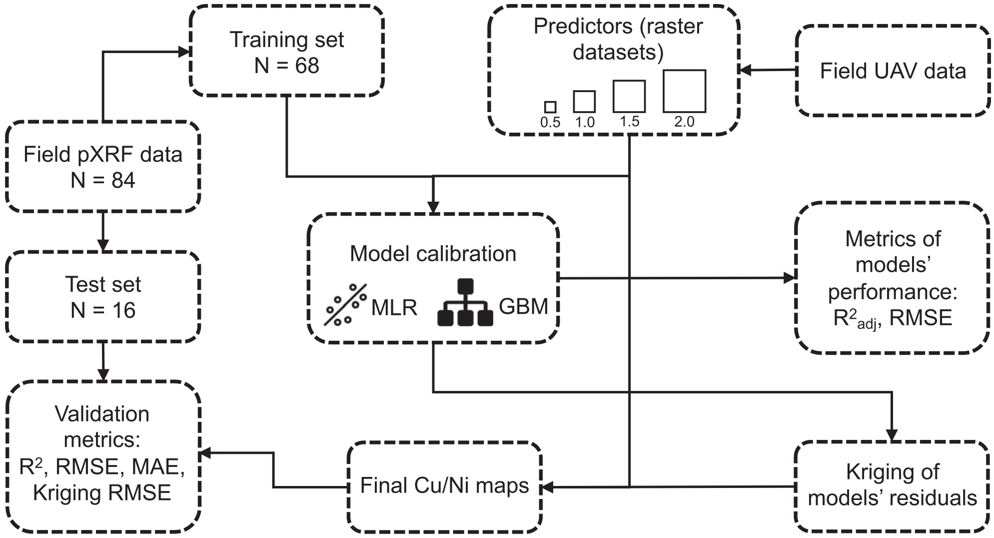


# 3 | RESULTS

## 3.1 | Field soil survey and XRF data

The soil survey allowed capturing variability in morphological and chemical properties, which was mainly explained by the determined soil types. Podzol profile lacked organic horizon (A) and the major part of elluvial (E) horizon, removed by intensive water erosion. A shallow illuvial ($B_{hs}$) horizon covered glacial parent materials with many stony inclusions. The previous remediation project based on covering degraded Podzol with a peat layer resulted in the formation of the Histosol/Podzol profile with the organic (RAT) horizon on the top of the Podzol profile described above. The profile of Histosols located in depression included two layers of peat, which differed in the level of organic matter decomposition. The ground water level was indicated at the 50 cm depth (Figure 3a). Soil formation and morphology resulted in a significant difference in soil properties. Total topsoil carbon content in Histosol was 60% higher than in Histosol/Podzol and more than four-times higher compared to Podzol (Figure 3b). The opposite pattern was reported for the bulk density: 1.13 (SD = 0.27) for Podzol compared to 0.45 (SD = 0.24) for Histosols and 0.62 (SD = 0.26) for Histosol/Podzol. Soil $pH_{H2O}$ ranged within 4.3–4.6 (95% confidence interval) with the minimal values for Histosols (Figure 3c). Soil factor explained 57% of the variance in carbon content and bulk density and 15% of the variance in pH (one-way ANOVA, $p$ <0.05).

In comparison to the background concentrations (0.005–0.007 g $kg^{-1}$ according to Kashulina (2017) the topsoil bulk content of Cu and Ni was 2–3 orders of magnitude higher at all observation points with the median values of 2.7 and 4.5 g $kg^{-1}$, respectively. Standard deviations (SD) were 1.98 and 5.28 g $kg^{-1}$, respectively. Training data for the regression ($n$ = 68, Cu: range 0.14–8.72 g $kg^{-1}$, median 2.76 g $kg^{-1}$, SD 1.89 g $kg^{-1}$; Ni: range 0.18–20.99 g $kg^{-1}$, median 4.85 g $kg^{-1}$, SD 5.18 g $kg^{-1}$) has a similar value distribution as the test dataset ($n$ = 16, Cu: range 0.46–9.0 g $kg^{-1}$, median 2.47 g $kg^{-1}$, SD 2.37 g $kg^{-1}$; Ni: range 0.53–17.48 g $kg^{-1}$, median 4.44 g $kg^{-1}$, SD 5.85 g $kg^{-1}$) as well as complete dataset. Square root transformed test data for Cu and Ni were distributed normally (Shapiro–Wilk normality test: $p$ = 0.37 for Cu, $p$ = 0.06 for Ni). The histogram for square root transformed Cu and Ni values is symmetrical with the bi-modal distribution of variables (Figure 4).

The Cu content had also high heterogeneity within samples of specific soil type: 0.14–3.76 for the Podzol, SD = 1.05; 1.13–5.71 for the Histosol/Podzol, SD = 1.41; and 2.06–9.04 for the Histosol, SD = 1.96. The Ni content (g $kg^{-1}$) was in the range of 0.18–16.83 in Podzol, SD = 3.81; 1.35–20.29 in Histosol/Podzol, SD = 5.65; and 4.25–21 in the Histosol, SD = 4.08.

## 3.2 | Environmental variables of the study site

The topography of the study site was presented by different geomorphological units. A hilltop covered by relocated peat and sparsely vegetated (Figure 5), hill slopes of various steepness up to 26° (Table 1), and flat depressions covered predominantly by Histosol (Figure 5). The absolute height range is relatively small (ca. 18 m), varying from 159 to 177 m (Figure 5b, Table 1). The characteristic feature of the study site is the microtopography – bedrock outcrops with overhydrated margins that are highly vulnerable to chemical weathering due to acidic precipitations in the vicinity of the smelter.

## 3.3 | Regression kriging

### 3.3.1 | Multiple linear regression and gradient boosting machines

The values of environmental variables for each training sampling point ($n$ = 68) were sampled from the DTM of four different spatial

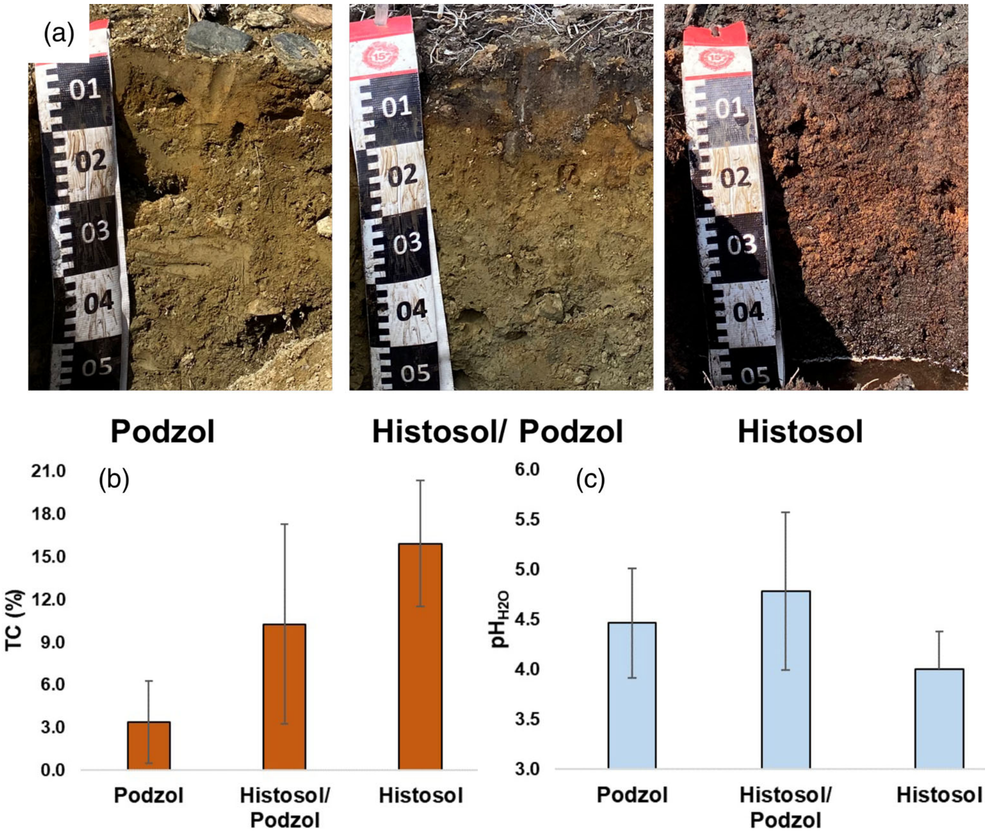


**FIGURE 3** Soil profiles and chemical properties [Colour figure can be viewed at wileyonlinelibrary.com]

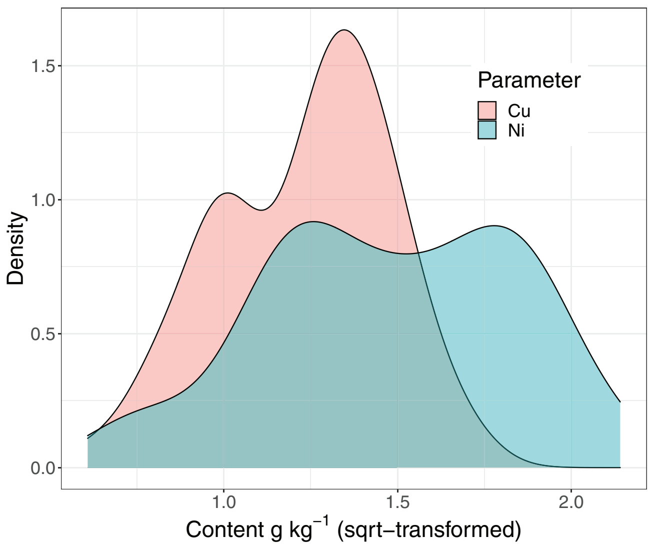


**FIGURE 4** Histogram distributions of the response variables (Cu and Ni contents in the topsoil [square root transformed]) [Colour figure can be viewed at wileyonlinelibrary.com]

resolutions (0.5–1.0–1.5–2.0 m). The spatial resolution had a particular effect on the final MLR and GBM models developed for these four datasets. All 16 final models (four – MLR and four – GBM for Cu and Ni, respectively) were statistically significant ($p$ <0.05). The soil type (difference between soils with high (Histosol, Histosol/Podzol) and low (Podzol) content of organic matter) was found to be an important variable explaining the considerable proportion of Cu and Ni variance in all models. Models have differed according to the list of other statistically significant topographic variables, and the overall percentage of the model's variance. The differences have been observed between models built for Cu and Ni at the same resolution DTM. In general, a higher $R^2_{adj}$ was estimated for Cu compared to Ni (Table 2).

### 3.3.2 | Mapping Cu and Ni content in the topsoil

Based on the obtained MLR and GBM models and fitted variograms, we created 16 maps of Cu and Ni contents (eight for each PTE) and have integrated all the maps into a single raster file as several raster bands. Raster statistics and calculated metrics for test points ($n$ = 16) are summarized in Table 3. Best validation metrics with optimal value ranges were obtained for Cu and Ni raster maps based on regression kriging with MLR/GBM models calculated for 1.0 and 1.5 m resolution DTM (Table 3). In general, MLR models significantly overestimated the upper limit of Cu and Ni contents of the study site, shifting it down with the decrease of raster resolution, but these overestimations did not exceed 0.3% of the total number of pixels and can be considered as outliers in our case. On the contrary, GBM models have shown very robust content ranges across all raster resolutions: Cu median content varied from 2.5 to 3.0 g kg$^{-1}$, and for Ni, these ranges were between 5.6 and 8.2 g kg$^{-1}$ (Table 3). Surprisingly, MLR models have shown better validation metrics compared to GBM: $R^2$ and RMSE of 0.7 and 1.41 versus 0.6 and 1.6 for Cu based on 1.5 m resolution; 0.43 and 4.29 versus 0.29

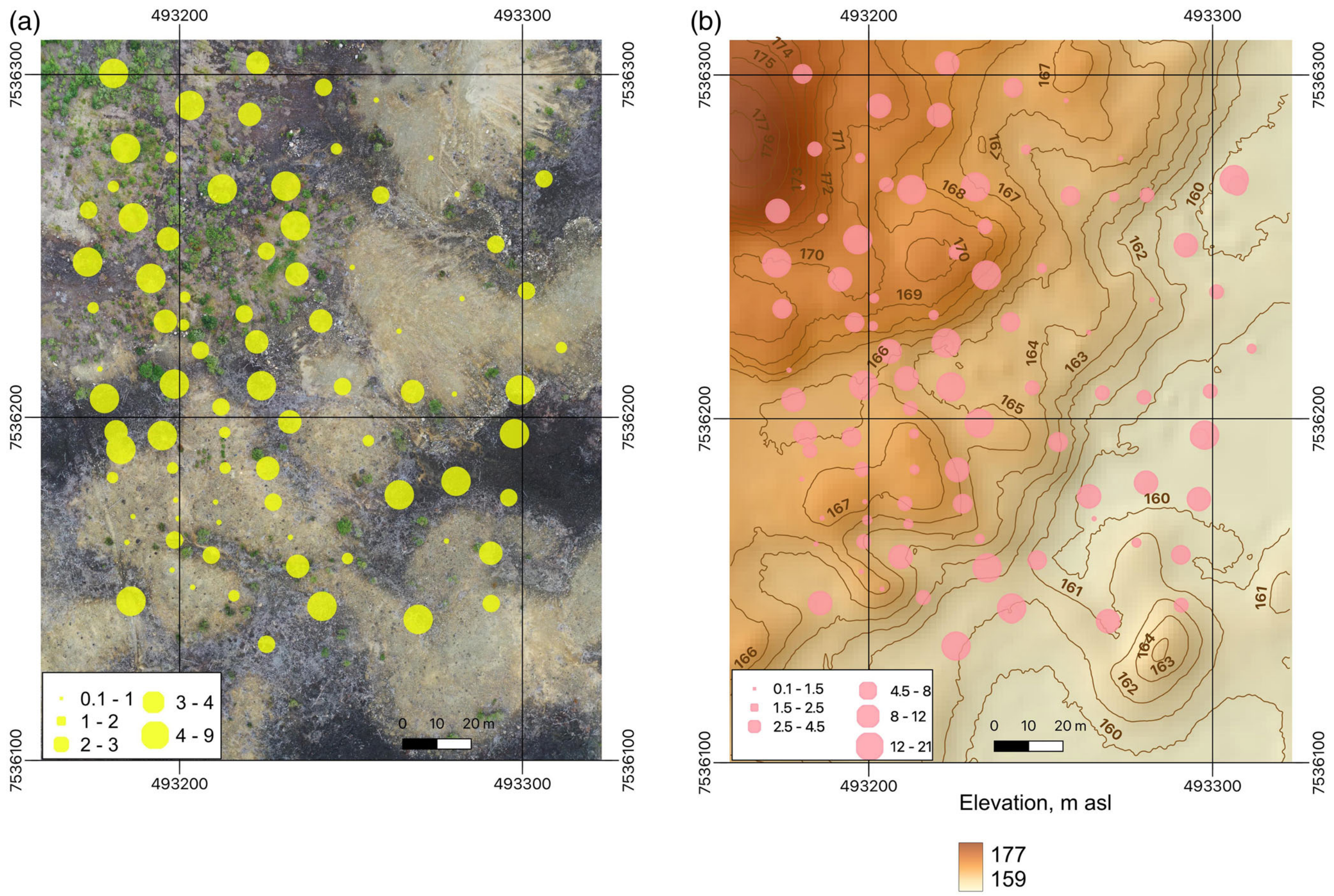


**FIGURE 5** Topographic representation of the study area and field-measured Cu and Ni content: (a) yellow circles: Cu content, g $kg^{-1}$, background: orthophoto of the study site exported from AGISOFT Metashape professional© software; (b) Rose circles: Ni content, g $kg^{-1}$, background: absolute heights of the study site (m asl) [Colour figure can be viewed at wileyonlinelibrary.com]

**TABLE 1** Summary table of prepared environmental variables

| Variable, unit | Range[a] | Mean[a] | Data type | Instrument |
|---|---|---|---|---|
| Elevation, m | 159.4–177.1 | 164.3 | float | UAV processing |
| Slopes, degrees | 0–26.5 | 6.7 | float | R *raster* (Robert & van Etten, 2012) |
| Aspect, degrees | 0–360 | 140.4 | float | - |
| Curvature | −0.1–0.7 | 0 | float | R *spatialEco* (Evans, 2020) |
| TWI | 4.0–16.2 | 6.7 | float | log(flowacc/tan[slope/180]) (Beven & Kirkby, 1979) |
| Flow direction | 1–128 | 24.4 | int | R *raster* (Robert & van Etten, 2012) |
| Flow accumulation (flowacc) | 2.2–5528.4 | 63.2 | float | R *dynatopmodel* (Quinn et al., 1995) |
| Soils | Histosol (1) – 29%<br>Histosol/Podzol (2) – 14%<br>Podzol (3) – 57% | | factor | Manual delineation from orthophoto + field descriptions |

[a]Range are calculated based on 1.5 m DTM; for other resolutions, ranges may insignificantly deviate.

and 4.77 for Ni-based on 1.0 m resolution. GBM based RK provided a smoother picture of Cu/Ni distribution maps (Figure 6b,d) compared to MLR based RK (Figure 6a,c). Although both models inherited the spatial structure of main predictors (soil type and TWI), GBM has been shown to perform better at the margins of different soil types and within these soil units. Validation metrics (Table 3) did not show any significant patterns of how raster resolution influences the quality of produced maps: $R^2$, RMSE and MAE varied in the same range both for Cu and Ni. And it is hard to conclude the best choice of raster resolution based on obtained validation metrics. Given the model performance analysis (Table 2) and validation metrics for Cu, we consider the input resolution of 1.5 m as optimal for such an area and sampling density.

**TABLE 2** Performance of obtained MLR and GBM models

| | Adjusted $R^2$ | | | | RMSE | | | |
|---|---|---|---|---|---|---|---|---|
| | MLR | | GBM | | MLR | | GBM | |
| Resolution, m | Cu | Ni | Cu | Ni | Cu | Ni | Cu | Ni |
| 0.5 | 0.51 | 0.48 | 0.69 | 0.43 | 0.38 | 0.70 | 0.19 | 0.61 |
| 1.0 | 0.56 | 0.39 | 0.56 | 0.34 | 0.36 | 0.76 | 0.29 | 0.66 |
| 1.5 | 0.56 | 0.43 | **0.76** | **0.55** | 0.36 | 0.74 | **0.16** | **0.54** |
| 2.0 | 0.50 | 0.45 | 0.72 | 0.49 | 0.38 | 0.72 | 0.18 | 0.58 |

*Note*: bold marked are best metrics among all models.

**TABLE 3** Summary of raster maps

| | | Content, g kg$^{-1}$ | | | | Metrics (validation), $n = 16$ | | |
|---|---|---|---|---|---|---|---|---|
| Resolution, m | Model | Min | Max | Med | Kriging RMSE | $R^2$ | MAE | RMSE |
| Cu | | | | | | | | |
| 0.5 | MLR | 0.0 | 124.0 | 2.0 | 0.16 | 0.55 | 1.23 | 1.57 |
| | GBM | 0.1 | 7.9 | 2.5 | **0.03** | 0.38 | 1.37 | 1.82 |
| 1.0 | MLR | 0.0 | 12.5 | 2.3 | 0.13 | 0.48 | 1.23 | 1.69 |
| | GBM | 0.2 | 6.7 | 2.5 | 0.08 | 0.35 | 1.30 | 1.87 |
| 1.5 | MLR | 0.0 | 16.4 | 2.6 | 0.14 | **0.70** | **0.89** | **1.41** |
| | GBM | 0.1 | 7.8 | 2.9 | **0.03** | 0.60 | 1.10 | 1.60 |
| 2.0 | MLR | 0.5 | 12.9 | 2.6 | 0.14 | 0.54 | 1.31 | 1.64 |
| | GBM | 0.1 | 8.3 | 3.0 | **0.03** | 0.37 | 1.44 | 1.86 |
| Ni | | | | | | | | |
| 0.5 | MLR | 0.0 | 455.3 | 5.1 | 0.51 | 0.39 | 3.40 | 4.42 |
| | GBM | 0.2 | 21.5 | 5.8 | 0.36 | 0.23 | 3.80 | 5.01 |
| 1.0 | MLR | 0.0 | 22.1 | 5.2 | 0.52 | **0.43** | **3.37** | **4.29** |
| | GBM | 0.2 | 17.5 | 5.6 | 0.40 | 0.29 | 3.68 | 4.77 |
| 1.5 | MLR | 0.6 | 30.8 | 6.0 | 0.58 | 0.28 | 3.55 | 4.94 |
| | GBM | 0.4 | 20.9 | 8.2 | **0.28** | 0.14 | 4.11 | 5.60 |
| 2.0 | MLR | 0.7 | 48.7 | 5.4 | 0.56 | 0.26 | 3.72 | 4.92 |
| | GBM | 0.2 | 22.0 | 7.0 | 0.34 | 0.24 | 3.68 | 5.04 |

*Note*: predictions of Cu and Ni content, as bold outlined are best metrics. The statistics is calculated for 135,432, 33,488, 14,766, 8137 pixels (resolution 0.5, 1, 1.5, 2 m respectively).

The topographic factor mainly explained high spatial variability in Cu and Ni contents within soil types captured by an intensive soil survey with pXRF. For example, the GBM model built upon 1.5 m resolution data showed a significant effect of TWI below 7.0 on Cu and Ni content. However, no influence was observed for the TWI above this value.

## 4 | DISCUSSION

### 4.1 | Distribution of Cu and Ni in the topsoil of the industrial barren impact area

The pollution mapping of the research area revealed high PTE contents (median Cu – 2.5 g kg$^{-1}$, Ni – 7.6 g kg$^{-1}$), which is in good coherence with the previous studies, reporting the content of Cu and Ni peaking to 6 and 9 g kg$^{-1}$, respectively (Kashulina, 2017). The outcomes are also comparable to the PTE contents reported for the heavily polluted 3 km buffer zone (Cu: 1.3–3.5 g kg$^{-1}$, Ni: 2.5–4.2 g kg$^{-1}$) (Evdokimova et al., 2011). Similar studies in the vicinity of the Sudbury smelters (Canada) also showed soil pollution by Cu and Ni, but in lower contents (max 1.3 g kg$^{-1}$ for Cu and 0.9 for Ni) (Dudka et al., 1995). The high correlation between Cu and Ni ($R = 0.86$) has also been found in samples from sites located in Sudbury, but the spatial gradient from the pollution source was not significant (Dudka et al., 1995).

Although the absolute values obtained by pXRF might deviate from the standard ICP-measurement, the revealed spatial patterns are robust (Qu et al., 2019). Besides, higher deviations are often shown for the small PTE contents close to detection limits, whereas for the highly polluted soil the pXRF results are relevantly accurate (Xia et al., 2019).

Soil variability has a substantial impact on the spatial patterns of PTE distribution both directly (e.g., via soil organic matter content, soil

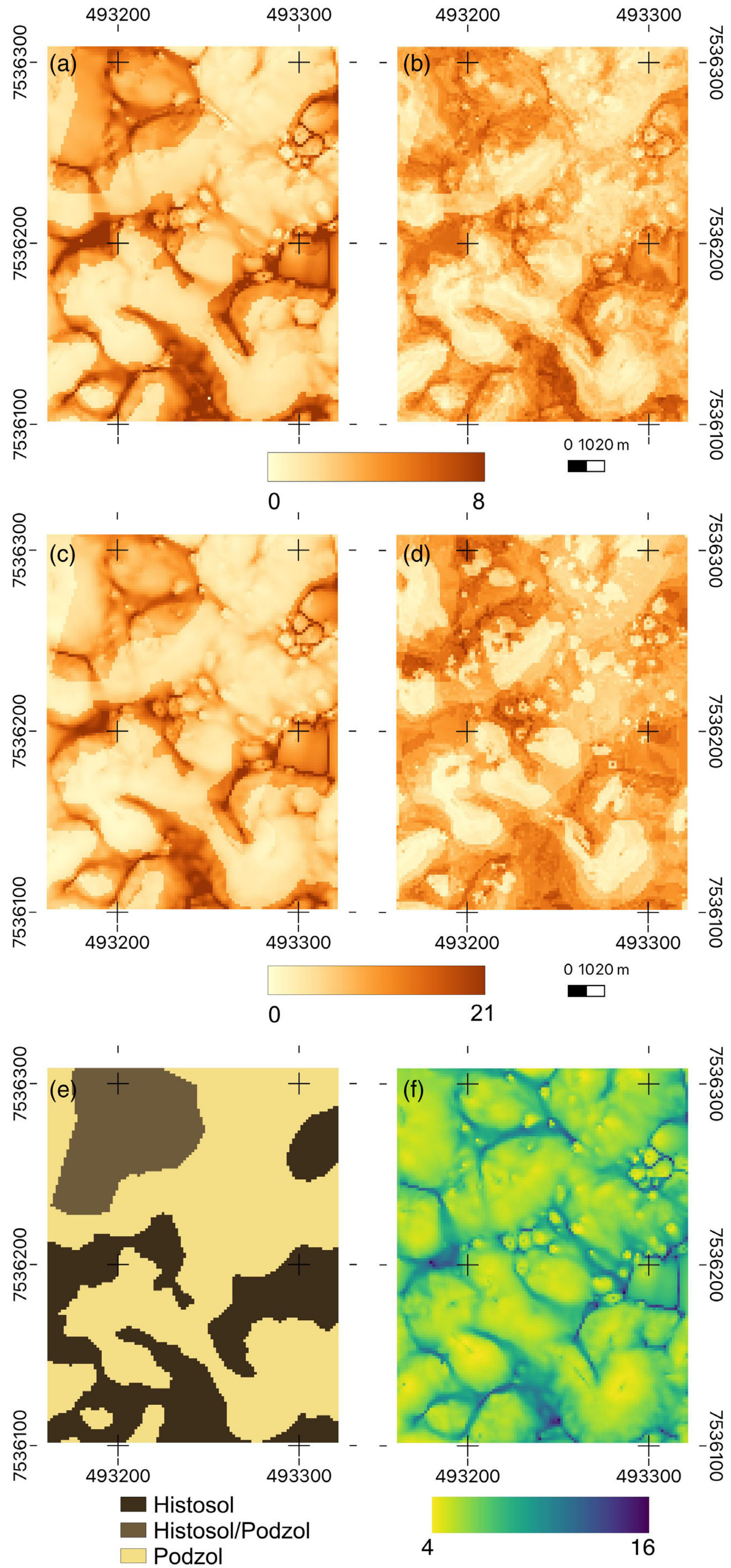


**FIGURE 6** Content of Cu and Ni in the topsoil (g $kg^{-1}$): (a),(b) Cu, (c),(d) Ni and important variables explaining its' spatial difference: (e) soil types, (f) TWI. Maps were obtained by regression kriging (MLR model input (a),(c) and GBM (b),(d) based on 1.5 m resolution dataset) [Colour figure can be viewed at wileyonlinelibrary.com]

moisture and buffer capacity) and indirectly (e.g., via soil catenas following the meso-topographic forms). In the research site, soil pollution decreased in a row: Histosol > Histosol/Podzol > Podzol. Topsoil organic matter content was the main influencing factor, which is also confirmed by a significant positive correlation with Cu and Ni contents (Paltseva et al., In press). Contents of Cu and Ni in Histosol/Podzol were lower than in Histosol due to its location on a flat hilltop and only 18-years of exposure to the smelter's emissions. Soil organic matter contributes to the metal accumulation by cation exchange, sorption, chelation, and complexing and overall to the increase of soil cation exchange capacity (Antoniadis et al., 2017; Lasota et al., 2020). The higher Cu content in the Histosol in comparison with the Podzol is explained both by the higher organic matter content and the low topographic position of Histosol. In Podzol, Ni was also likely absorbed by the clay particles. As a result, the Ni content range in Podzol was nearly the same as in the Histosol and Histosol/Podzol (Lyanguzova et al., 2015; Slukovskaya, Kremenetskaya, et al., 2020; Slukovskaya, Vasenev, et al., 2020; Vodyanitsky, 2008). Besides, Histosol and Histosol/Podzol are less exposed to erosion compared to the Podzol due to higher water holding capacity and a denser vegetation cover. High soil moisture in the Histosol could affect the accuracy of the pXRF measurements. However, unlikely this effect was considerable. The previous studies (Paltseva et al., In press; Xia et al., 2019) showed that water content had an impact on detecting low concentrations of PTEs (below 0.1 g kg$^{-1}$), whereas for the very high concentrations found at the industrial barren it is unlikely that this effect can be significant.

Since we have observed the influence of TWI in the range of 5.5–7.0, Cu and Ni distributions were mainly driven by topography at the hilltops and relatively steep slopes, whereas in depressions and gentle slopes with high accumulation potential, the soil type was the dominating factor. Traditionally, TWI is a widely used predictor in digital soil mapping, but it is rather used at the regional scale for the PTE mapping than at the local scale comparable to our research site (Cao et al., 2017; Wu et al., 2020). In one of the local scale studies, the influence of TWI on topsoil Cu and Ni contents was found insignificant, at least for the 5 m resolution DEM and low metal contents (Duan et al., 2015). Based on the spatial patterns of Cu/Ni contents described in the literature and based on the outcomes of our models, the relevance of TWI as a predictor for the PTE mapping can be limited by 1) application to polluted areas: saturation point can highlight pathways of lateral element transport (Kashulina, 2017); 2) calculation based on optimal DTM resolution (Hengl, 2006) (lower DTM resolution smooths the differences among pixels, and exhaustive DTM resolution may also result in minimizing its importance [Florinsky & Kuryakova, 2000]). We suggest paying particular attention to the initial DTM resolution. At the finest resolution (0.5 m), TWI had not played a considerable role and was replaced by curvature in our models. The lowest curvature values (concave patterns) corresponded to the higher Cu and Ni contents, but the reverse relationship could only be traced for curvature values between $-0.02$ and 0.02, representing flat terrain. Other changes in Cu and Ni contents were explained by soil type at this resolution level (0.5 m). In general, GBM models calculated for all DTM resolutions (0.5–1.0–1.5–2 m) revealed the same effect of soil type and topography on the content of Cu and Ni in topsoil: significant difference between Podzol (low content) and Histosol/ Histosol/Podzol (high content) enhanced by topographic patterns with the highest contents at locations where lateral accumulation is expected.

## 4.2 | Applicability of regression kriging for mapping PTE content in soils with a limited sample size

Field data limitation is a challenge to implement the kriging. However, the minimal sample size depends on the research area and purpose of the study (Hartemink et al., 2008). For example, global and regional maps are usually based on thousands of samples (e.g., Stoorvogel et al., 2017; Xie et al., 2011), whereas at the regional and local scale a hundred is a more typical sample size (Richter et al., 2020; Romzaykina et al., 2021). Soil pollution assessment also likely requires a smaller dataset than, for example, precise agriculture (Roberton et al., 2020). Our study was focused on the catchment area of a total of two ha, resulting in over 40 samples per ha, which is comparable to many digital soil mapping studies (von Steiger et al., 1996; Zhang & Yang, 2020) and considerably higher than recommended for the conventional soil survey at the polluted sites in Russia (Savich & Gataulin, 2010).

The spatial relationships between PTE and environmental predictors quantified for the study can be further extrapolated to the entire impact zone (up to 3 km away from the smelter) (Evdokimova et al., 2011) using the UAV-based DTM & RK approach. In general, topographic variables have been widely used for mapping soil parameters as independent input variables (Agyeman et al., 2021; Florinsky et al., 2002; Minasny & McBratney, 2016; Moore et al., 1991). Indeed, within-catchment processes, including lateral transport pathways of water and sediments, can closely be related to topography and its derivatives of a different order (Moore et al., 1991). The mapping is generally based on finding statistically significant relationships between the soil parameters and additional topographic variables. Nevertheless, the choice of the optimal output raster resolution/or input auxiliary maps is crucial in such tasks (Florinsky & Kuryakova, 2000; Hengl, 2006). With the decrease of input DTM spatial resolution the predictive power of a particulate terrain parameter/environmental variable can be lost (Thompson & Moore, 1996) or the correlation between them can turn from logically negative to illogically positive (Florinsky & Kuryakova, 2000). These cases can be observed if the small-scale variability of the response variable surpasses the variability of explanatory variable (i.e., resampling to lower raster resolution would lead to inadequate relations between response and explanatory variables). Since the study site can be characterized as catchment-scale, we have tested the application of hydrologically correct DTMs with various resolutions (0.5–1.0–1.5–2 m) obtained by interpolation of cleaned UAV-derived contours (Hutchinson, 1989), trying to avoid any uncertainties caused by DTM input resolution. The decision of this resolution range is based on the i) finest possible resolution of UAV-derived data given the vertical accuracy (0.5 m); ii) the optimal output interpolation resolution (1.5 m) calculated given the initial inspection density for the study site, as described in Hengl (2006). In our research, we considered the input DTM and output interpolation resolution of 1.5 m as optimal, given the initial models' performance and calculated metrics at the validation stage for Cu (MLR-based interpolation) (Table 3). The best validation metrics were estimated for interpolated Cu and Ni maps based on 1.0 and 1.5 m datasets MLR/GBM RK: the highest correlation between interpolated and observed content values ($n = 16$) and the lowest MAE and RMSE values (Table 3). In general, the interpolation results for Cu can be considered as satisfactory and marginally satisfactory for Ni (Lado et al., 2008).

At all levels of resolution, we have obtained the similar relationships between Cu/Ni content and soil type and TWI (1.0–1.5–2.0 m)/ curvature (0.5 m), suggesting that at all these levels, the obtained nonlinear (and linear) regression models are stable and robust. Perhaps, the application of coarser-resolution input DTM would lead to inadequate Cu/Ni content – topography relations within a specific soil type (e.g., higher content observed at pixels with lower TWI) as it is described in Florinsky & Kuryakova (2000).

The spatial interpolation approach in this study is considered as combined (i.e. statistical regression + geostatistics) (Li & Heap, 2014; Zhu & Lin, 2010). The observed influence patterns of soil type and TWI on Cu and Ni content suggest that simple geostatistical methods (e.g., ordinary kriging) cannot be used for tracing the spatial dynamic of these soil parameters in our case. In fact, Cu/Ni content in the topsoil of industrial barren is closely related to auxiliary data, which are important for understanding relationships between soil properties and other environmental variables that can be considered for further remediation measures (Lado et al., 2008). The disadvantage of MLR models within regression kriging, observed in this study, is the prediction uncertainties caused by an overestimation of interpolated parameters (Table 3) and the mapping issues reflected in sharp changes in PTE concentrations at the margins of soil units, which is incorrect from the geographical point of view (Figure 6a,c). Herewith, the validation metrics of MLR-based maps are comparable or even better than GBM-based interpolations (Table 3). The GBM models have a certain advantage over MLR since it can deal with non-linearities between dependent and explanatory variables (Elith et al., 2008). Despite the simple geostatistical methods (ordinary kriging) still prevail in studies devoted to mapping PTE in soils (Agyeman et al., 2021), the application of GBM (stand-alone and within regression kriging) shows promising results in this field and, in conjunction with other machine learning methods, deserves special attention (Li & Heap, 2014).

This study has shown that the fine-scale auxiliary data obtained from the UAV survey (topography, soil types) can successfully be used in RK of Cu and Ni content in topsoil. The obtained maps of Cu and Ni distribution can further be extended for the larger areas and might be helpful for the planning of remediation procedures at these heavily polluted areas.

## 5 | CONCLUSIONS

High-resolution maps of the potentially toxic element contents in the industrial barren topsoils in the Russian SubArctic were obtained by integrating remote sensing and soil proximal sensing. The UAV-derived soil/terrain parameters, including soil type, topographic wetness index, curvature and slopes explained 55% to 76% of the total variance in Cu and Ni content based on gradient boosting machines. Compared to Podzol, Histosol had significantly higher concentrations of Cu and Ni due to sorption by organic matter and accumulation due to soil erosion and low position in relief. The spatial distribution of Cu and Ni within the soil types was mainly driven by the lateral transport processes and therefore was explained by the topographic wetness index. Interpolation of the obtained spatial relationships by the regression kriging allowed comparing different input models (multiple linear regression and gradient boosting machines) as well as resolution levels of the input data. The most accurate mapping of Cu and Ni contents was achieved by applying a 1.5 m resolution dataset. The tested methodology is foreseen to have a future-wide implementation in semi-automated/fully automated mapping of soil pollution. UAV survey over the larger area or analysis of available high-resolution DEM (e.g., ArcticDEM) could allow further extrapolation of the potentially toxic element contents for the whole industrial barren to support the prospective remediation projects.

### ACKNOWLEDGMENTS

Soil survey and analysis were supported by the Russian Foundation for Basic Research - Project #19-29-05187. Remote sensing and modeling were supported by Russian Science Foundation - Project #19-77-300-12. Data analysis (Y.Dvornikov, M.Slukovskaya, A. Yaroslavtsev, D.Sarzhanov) and paper preparation (Y.Dvornikov, M. Slukovskaya) were supported by the RUDN University Strategic Academic Leadership Program.

### CONFLICT OF INTEREST

The authors declare no conflict of interest.

### AUTHOR CONTRIBUTIONS

Conceptualization, Vyacheslav Vasenev and Yury Dvornikov; methodology, Yury Dvornikov and Joulia Meshalkina; software, Alexey Yaroslavtsev; validation, Yury Dvornikov, Marina Slukovskaya; formal analysis, Yury Dvornikov; investigation, Yury Dvornikov, Marina Slukovskaya, Alexey Ryazanov, Dmitrii Sarzhanov, Alexey Yaroslavtsev, Vyacheslav Vasenev; resources, Alexey Yaroslavtsev, Vyacheslav Vasenev; data curation, Alexey Ryazanov, Dmitrii Sarzhanov, Yury Dvornikov, Marina Slukovskaya; writing—original draft preparation, Yury Dvornikov, Marina Slukovskaya; writing—review and editing, Yury Dvornikov, Marina Slukovskaya; supervision, Vyacheslav Vasenev; project administration, Vyacheslav Vasenev; funding acquisition, Vyacheslav Vasenev.

### DATA AVAILABILITY STATEMENT

The data that support the findings of the study are available upon request from the corresponding author.

## ORCID

*Yury Dvornikov* https://orcid.org/0000-0003-3491-4487
*Marina Slukovskaya* https://orcid.org/0000-0002-5406-5569
*Alexey Yaroslavtsev* https://orcid.org/0000-0003-4115-3233
*Joulia Meshalkina* https://orcid.org/0000-0003-1513-2439
*Dmitrii Sarzhanov* https://orcid.org/0000-0002-1627-2487
*Vyacheslav Vasenev* https://orcid.org/0000-0003-0286-3021

## REFERENCES

Agyeman, P. C., Ahado, S. K., Borůvka, L., Biney, J. K. M., Sarkodie, V. Y. O., Kebonye, N. M., & Kingsley, J. (2021). Trend analysis of global usage of digital soil mapping models in the prediction of potentially toxic elements in soil/sediments: A bibliometric review. *Environmental Geochemistry and Health*, *43*. 1715–1739. https://doi.org/10.1007/s10653-020-00742-9

Antoniadis, V., Levizou, E., Shaheen, S. M., Ok, Y. S., Sebastian, A., Baum, C., Majeti, N. V., Prasad, W., Wenzel, W., & Rinklebe, J. (2017). Trace elements in the soil-plant interface: Phytoavailability, translocation, and phytoremediation–a review. *Earth-Science Reviews*, *171*, 621–645. https://doi.org/10.1016/j.earscirev.2017.06.005

Beck, H. E., Zimmermann, N. E., McVicar, T. R., Vergopolan, N., Berg, A., & Wood, E. F. (2018). Present and future Köppen-Geiger climate classification maps at 1-km resolution. *Scientific Data*, *5*, 180214. https://doi.org/10.1038/sdata.2018.214

Beven, K. J., & Kirkby, M. J. (1979). A physically based, variable contributing area model of basin hydrology. *Hydrological Sciences Bulletin*, *24*(1), 43–69. https://doi.org/10.1080/02626667909491834

Boente, C., Salgado, L., Romero-Macias, E., Colina, A., Lopez-Sanchez, C., & Gallego, J. L. R. (2020). Correlation between geochemical and multispectral patterns in an area severely contaminated by former hg-as mining. *ISPRS International Journal of Geo-Information*, *9*, 739. https://doi.org/10.3390/ijgi9120739

Cao, S., Lu, A., Wang, J., & Huo, L. (2017). Modeling and mapping of cadmium in soils based on qualitative and quantitative auxiliary variables in a cadmium contaminated area. *Science of the Total Environment*, *580*, 430–439. https://doi.org/10.1016/j.scitotenv.2016.10.088

Duan, X., Zhang, G., Rong, L., Fang, H., He, D., & Feng, D. (2015). Spatial distribution and environmental factors of catchment-scale soil heavy metal contamination in the dry-hot valley of upper Red River in southwestern China. *Catena*, *135*, 59–69. https://doi.org/10.1016/j.catena.2015.07.006

Dudka, S., Ponce-Hernandez, R., & Hutchinson, T. C. (1995). Cirrent level of total element concentration in the surface layer of Sudbury's soils. *Science of the Total Environment*, *162*, 161–171.

Elith, J., Leathwick, J. R., & Hastie, T. (2008). A working guide to boosted regression trees. *Journal of Animal Ecology*, *77*, 802–813. https://doi.org/10.1111/j.1365-2656.2008.01390.x

Evans, J. S. (2020). *R spatialEco-package* (1.3-1). https://github.com/jeffreyevans/spatialEco

Evdokimova, G. A., Kalabin, G. V., & Mozgova, N. P. (2011). Contents and toxicity of heavy metals in soils of the zone affected by aerial emissions from the Severonikel Enterprise. *Eurasian Soil Science*, *44*(2), 237–244. https://doi.org/10.1134/S1064229311020037

Florinsky, I. V., Eilers, R. G., Manning, G. R., & Fuller, L. G. (2002). Prediction of soil properties by digital terrain modelling. *Environmental Modelling and Software*, *17*(3), 295–311. https://doi.org/10.1016/S1364-8152(01)00067-6

Florinsky, I. V., & Kuryakova, G. A. (2000). Determination of grid size for digital terrain modelling in landscape investigations—Exemplified by soil moisture distribution at a micro-scale. *International Journal of Geographical Information Science*, *14*(8), 815–832. https://doi.org/10.1080/136588100750022804

Gholizadeh, A., & Kopačková, V. (2019). Detecting vegetation stress as a soil contamination proxy: A review of optical proximal and remote sensing techniques. *International journal of Environmental Science and Technology*, *16*, 2511–2524. https://doi.org/10.1007/s13762-019-02310-w

Gräler, B., Pebesma, E., & Heuvelink, G. (2016). Spatio-temporal interpolation using gstat. *The R Journal*, *8*(1), 204–218. https://doi.org/10.32614/RJ-2016-014

Guo, Y., Huang, J., Shi, Z., & Li, H. (2015). Mapping spatial variability of soil salinity in a coastal paddy field based on electromagnetic sensors. *PLoS ONE*, *10*(5), e0127996. https://doi.org/10.1371/journal.pone.0127996

Hartemink, A. E., McBratney, A., & Mendonça-Santos, M. L. (2008). *Digital soil mapping with limited data*. Berlin: Springer. https://doi.org/10.1007/978-1-4020-8592-5

Hengl, T. (2006). Finding the right pixel size. *Computers and Geosciences*, *32*, 1283–1298. https://doi.org/10.1016/j.cageo.2005.11.008

Hong, Y., Shen, R., Cheng, H., Chen, Y., Zhang, Y., Liu, Y., Zhou, M., Yu, L., Liu, Y., & Liu, Y. (2019). Estimating lead and zinc concentrations in peri-urban agricultural soils through reflectance spectroscopy: Effects of fractional-order derivative and random forest. *Science of the Total Environment*, *651*, 1969–1982. https://doi.org/10.1016/j.scitotenv.2018.09.391

Hutchinson, M. F. (1989). A new procedure for gridding elevation and stream line data with automatic removal of spurious pits. *Journal of Hydrology*, *106*, 211–232. https://doi.org/10.1016/0022-1694(89)90073-5

IUSS Working Group WRB (2015). World Reference Base for Soil Resources 2014, update 2015. International soil classification system for naming soils and creating legends for soil maps. In *World Soil Resources Reports No. 106*. Rome: FAO. https://www.fao.org/3/i3794en/I3794en.pdf

Jenson, S. K., & Domingue, J. O. (1988). Extracting topographic structure from digital elevation data for geographic information system analysis. *Photogrammetric Engineering and Remote Sensing*, *54*(11), 1593–1600.

Kalnicky, D. J., & Singhvi, R. (2001). Field portable XRF analysis of environmental samples. *Journal of Hazardous Materials*, *83*(1–2), 93–122. https://doi.org/10.1016/S0304-3894(00)00330-7

Kashulina, G. M. (2017). Extreme pollution of soils by emissions of the copper–nickel industrial complex in the Kola Peninsula. *Eurasian Soil Science*, *50*, 837–849. https://doi.org/10.7868/s0032180x17070036

Kashulina, G. M. (2018). Monitoring of soil contamination by heavy metals in the impact zone of copper-nickel smelter on the Kola peninsula. *Eurasian Soil Science*, *51*, 467–478. https://doi.org/10.7868/s0032180x1804010x

Koptsik, G. N., Koptsik, S. V., & Smirnova, I. E. (2016). Alternative technologies for remediation of technogenic barrens in the Kola subArctic. *Eurasian Soil Science*, *49*(11), 1294–1309. https://doi.org/10.1134/S1064229316090088

Kozlov, M. V., & Zvereva, E. L. (2007). Industrial barrens: Extreme habitats created by non-ferrous metallurgy. *Reviews in Environmental Science and Biotechnology*, *6*, 231–259. https://doi.org/10.1007/s11157-006-9117-9

Kryuchkov, V. V. (1993). Extreme anthropogenic loads and the northern ecosystem condition. *Ecological Applications*, *3*(4), 622–630. https://doi.org/10.2307/1942095

Lado, L. R., Hengl, T., & Reuter, H. I. (2008). Heavy metals in European soils: A geostatistical analysis of the FOREGS geochemical database. *Geoderma*, *148*, 189–199. https://doi.org/10.1016/j.geoderma.2008.09.020

Lasota, J., Błońska, E., Łyszczarz, S., & Tibbett, M. (2020). Forest humus type governs heavy metal accumulation in specific organic matter fractions. *Water, Air, & Soil Pollution*, *231*(2), 1–13. https://doi.org/10.1007/s11270-020-4450-0

Li, J., & Heap, A. D. (2014). Spatial interpolation methods applied in the environmental sciences: A review. *Environmental Modelling and Software*, *53*, 173–189. https://doi.org/10.1016/j.envsoft.2013.12.008

Lyanguzova, I. V., Goldvirt, D. K., & Fadeeva, I. K. (2015). Transformation of polymetallic dust in the organic horizon of Al-Fe-humus Podzol (field experiment). *Eurasian Soil Science*, *48*(7), 701–711. https://doi.org/10.1134/S1064229315050051

Lyanguzova, I. V., Goldvirt, D. K., & Fadeeva, I. K. (2016). Spatiotemporal dynamics of the pollution of Al–Fe-humus Podzols in the impact zone of a nonferrous metallurgical plant. *Eurasian Soil Science*, *49*(10), 1189–1203. https://doi.org/10.1134/S1064229316100094

Manninen, S., Zverev, V., Bergman, I., & Kozlov, M. (2015). Consequences of long-term severe industrial pollution for above ground carbon and nitrogen pools in northern taiga forests at local and regional scales. *Science of the Total Environment*, *536*, 616–624. https://doi.org/10.1016/j.scitotenv.2015.07.097

Minasny, B., & McBratney, A. B. (2016). Digital soil mapping: A brief history and some lessons. *Geoderma*, *264*, 301–311. https://doi.org/10.1016/j.geoderma.2015.07.017

Moore, I. D., Grayson, R. B., & Ladson, A. R. (1991). Digital terrain modelling: A review of hydrological, geomorphological, and biological applications. *Hydrological Processes*, *5*(1), 3–30. https://doi.org/10.1002/hyp.3360050103

Nikanov, A. N., Dorofeev, V. M., Megorskiy, V. V., & Zhirov, V. K. (2020). *Environmental aspects of the accumulation of mineral elements in the organism of the population living in areas of intensive industrial activities in the European part of the Arctic zone of Russia*, FRC KSC RAS. (87). Apatity: FRC KSC RAS.

Nouri, H., Borujeni, S. C., Alaghmand, S., Anderson, S. J., Sutton, P. C., Parvazian, S., & Beecham, S. (2018). Soil salinity mapping of urban greenery using remote sensing and proximal sensing techniques; the case of Veale Gardens within the Adelaide Parklands. *Sustainability*, *10*(8), 2826. https://doi.org/10.3390/su10082826

Paltseva, A., Slukovskaya, M. V., Romzaykina, O. N., Sarzhanov, D. A., Drogobuzhskaya, S. V., Dvornikov, Y. A., & Vasenev, V. I. (In press). Proximal sensing of soil pollution by heavy metals using a portable X-ray fluorescence analyzer in subArctic industrial barren: Limitations and perspectives. In A. Rakshit, S. Ghosh, V. I. Vasenev, H. Pathak, & V. D. Rajput (Eds.), *Soils in Urban Ecosystem*. Cham: Springer Singapore In press.

Qu, M., Chen, J., Li, W., Zhang, C., Wan, M., Huang, B., & Zhao, Y. (2019). Correction of in-situ portable X-ray fluorescence (PXRF) data of soil heavy metal for enhancing spatial prediction. *Environmental Pollution*, *254*, 112993. https://doi.org/10.1016/j.envpol.2019.112993

Quinn, P., Beven, K. J., & Lamb, R. (1995). The in (a/tan/beta) index: How to calculate it and how to use it within the Topmodel framework. *Hydrological Processes*, *9*(2), 161–182.

R Core Team. (2017). *R: A language and environment for statistical computing (4.0.5)*. Vienna: R Foundation for Statistical Computing. https://www.r-project.org/

Richter, S., Haase, D., Thestorf, K., & Makki, M. (2020). Carbon pools of Berlin, Germany: Organic carbon in soils and aboveground in trees. *Urban Forestry & Urban Greening*, *54*, 126777. https://doi.org/10.1016/j.ufug.2020.126777

Robert, J. H., & van Etten, J. (2012). *R-package raster: Geographic analysis and modeling with raster data* (2.0–12). http://cran.r-project.org/package=raster

Roberton, S. D., Bennett, J. M., Lobsey, C. R., & Bishop, T. F. A. (2020). Assessing the sensitivity of site-specific lime and gypsum recommendations to soil sampling techniques and spatial density of data collection in Australian agriculture: A pedometric approach. *Agronomy*, *10*(11), 1676. https://doi.org/10.3390/agronomy10111676

Romzaykina, O. N., Vasenev, V. I., Paltseva, A., Kuzyakov, Y. V., Neaman, A., & Dovletyarova, E. A. (2021). Assessing and mapping urban soils as geochemical barriers for contamination by heavy metal(loid)s in Moscow megapolis. *Journal of Environmental Quality*, *50*. 22–37. https://doi.org/10.1002/jeq2.20142

Sacristán, D., Viscarra Rossel, R. A., & Recatalá, L. (2016). Proximal sensing of Cu in soil and lettuce using portable X-ray fluorescence spectrometry. *Geoderma*, *265*, 6–11. https://doi.org/10.1016/j.geoderma.2015.11.008

Savich, V. I., & Gataulin, A. M. (2010). In *Land valuation*. (448). Moscow: VNIIA.

Shi, T., Guo, L., Chen, Y., Wang, W., Shi, Z., Li, Q., & Wu, G. (2018). Proximal and remote sensing techniques for mapping of soil contamination with heavy metals. *Applied Spectroscopy Reviews*, *53*(10), 783–805. https://doi.org/10.1080/05704928.2018.1442346

Slukovskaya, M. V., Kremenetskaya, I. P., Drogobuzhskaya, S. V., & Novikov, A. I. (2020). Sequential extraction of potentially toxic metals: Alteration of method for Cu-Ni polluted peat soil of industrial barren. *Toxics*, *8*(39), 1–10. https://doi.org/10.3390/TOXICS8020039

Slukovskaya, M. V., Vasenev, V. I., Ivashchenko, K. V., Dolgikh, A. V., Novikov, A. I., Kremenetskaya, I. P., Ivanova, L. A., & Gubin, S. V. (2020). Organic matter accumulation by alkaline-constructed soils in heavily metal-polluted area of subArctic zone. *Journal of Soils and Sediments*. *21*, 2071–2088. https://doi.org/10.1007/s11368-020-02666-4

Slukovskaya, M. V., Vasenev, V. I., Ivashchenko, K. V., Morev, D., Drogobuzhskaya, S., Ivanova, L., & Kremenetskaya, I. P. (2019). Technosols on mining wastes in the subarctic: Efficiency of remediation under Cu-Ni atmospheric pollution. *International Soil and Water Conservation Research*, *7*, 297–307. https://doi.org/10.1016/j.iswcr.2019.04.002

Stoorvogel, J. J., Bakkenes, M., Temme, A. J. A. M., Batjes, N. H., & ten Brink, B. J. E. (2017). S-world: A global soil map for environmental modelling. *Land Degradation & Development*, *28*(1), 22–33. https://doi.org/10.1002/ldr.2656

Tan, K., Wang, H., Chen, L., Du, Q., Du, P., & Pan, C. (2020). Estimation of the spatial distribution of heavy metal in agricultural soils using airborne hyperspectral imaging and random forest. *Journal of Hazardous Materials*, *382*, 120987. https://doi.org/10.1016/j.jhazmat.2019.120987

Thompson, J. C., & Moore, R. D. (1996). Relations between topography and water table depth in a shallow forest soil. *Hydrological Processes*, *10*(11), 1513–1525. https://doi.org/10.1002/(sici)1099-1085(199611)10:11<1513::aid-hyp398>3.0.co;2-v

Vodyanitsky, Y. N. (2008). Affinity of heavy metals and metalloids for carriers in soils. *Agrokhimia*, *9*, 87–94.

von Steiger, B., Webster, R., Schulin, R., & Lehmann, R. (1996). Mapping heavy metals in polluted soil by disjunctive kriging. *Environmental Pollution*, *94*(2), 205–215. https://doi.org/10.1016/S0269-7491(96)00060-7

Wadoux, A. M. J. C., & Brus, D. J. (2021). How to compare sampling designs for mapping? *European Journal of Soil Science*, *72*, 35–46. https://doi.org/10.1111/ejss.12962

Wu, Z., Chen, Y., Han, Y., Ke, T., & Liu, Y. (2020). Identifying the influencing factors controlling the spatial variation of heavy metals in suburban soil using spatial regression models. *Science of the Total Environment*, *717*, 137212. https://doi.org/10.1016/j.scitotenv.2020.137212

Xia, F., Hu, B., Shao, S., Xu, D., Zhou, Y., Zhou, Y., Huang, M., Li, Y., Chen, S., & Shi, Z. (2019). Improvement of spatial modeling of Cr, Pb, cd, as and Ni in soil based on portable X-ray fluorescence (PXRF) and geostatistics: A case study in East China. *International Journal of Environmental Research and Public Health*, *16*(15), 2694. https://doi.org/10.3390/ijerph16152694

Xie, Y., Chen, T. B., Lei, M., Yang, J., Guo, Q. J., Song, B., & Zhou, X. Y. (2011). Spatial distribution of soil heavy metal pollution estimated by different interpolation methods: Accuracy and uncertainty analysis. *Chemosphere*, *82*(3), 468–476. https://doi.org/10.1016/j.chemosphere.2010.09.053

Zeverbergen, L. W., & Thorne, C. R. (1987). Quantitative analysis of land surface topography. *Earth Surface Processes and Landforms*, *12*(1), 47–56. https://doi.org/10.1002/esp.3290120107

Zhang, C., & Yang, Y. (2020). Modeling the spatial variations in anthropogenic factors of soil heavy metal accumulation by geographically weighted logistic regression. *Science of the Total Environment*, *717*, 137096. https://doi.org/10.1016/j.scitotenv.2020.137096

Zhu, Q., & Lin, H. S. (2010). Comparing ordinary kriging and regression kriging for soil properties in contrasting landscapes. *Pedosphere*, *20*(5), 594–606. https://doi.org/10.1016/S1002-0160(10)60049-5

**How to cite this article:** Dvornikov, Y., Slukovskaya, M., Yaroslavtsev, A., Meshalkina, J., Ryazanov, A., Sarzhanov, D., & Vasenev, V. (2022). High-resolution mapping of soil pollution by Cu and Ni at a polar industrial barren area using proximal and remote sensing. *Land Degradation & Development*, 1–14. https://doi.org/10.1002/ldr.4261